IOP PUBLISHING JOURNAL OF PHYSICS D: APPLIED PHYSICS

J. Phys. D: Appl. Phys. **42** (2009) 214011 (12pp) doi:10.1088/0022-3727/42/21/214011

Interaction and coalescence of nanovoids and dynamic fracture in silica glass: multimillion-to-billion atom molecular dynamics simulations

Ken-ichi Nomura[1], Yi-Chun Chen[1], Wang Weiqiang[1], Rajiv K Kalia[1], Aiichiro Nakano[1], Priya Vashishta[1] and Lin H Yang[2]

[1] Collaboratory for Advanced Computing and Simulations, University of Southern California, Los Angeles, CA, 90089-0242 USA

[2] Physics/H Division, Lawrence Livermore National Laboratory, Livermore, CA, 94551 USA

Received 23 March 2009, in final form 24 March 2009
Published 22 October 2009
Online at stacks.iop.org/JPhysD/42/214011

Abstract

In this review, we present our recent results for atomistic mechanisms of damage nucleation and growth and dynamic fracture in silica glass. These results have been obtained with multimillion-to-billion atom, parallel, molecular dynamics simulations of (1) the interaction and coalescence of nanovoids in amorphous silica subjected to dilatational strain and (2) the nucleation, growth and healing of wing cracks and damage nanocavities in silica glass under impact loading. We also give an overview of our current efforts to perform dynamic fracture simulations over microsecond time scales and multiscale simulations of stress corrosion cracking in silica glass.

1. Introduction

Silica glass is often thought of as a prototype brittle material [1]. The conventional view of failure in silica glass under tensile loading is that a crack propagates by breaking Si–O bonds. This failure scenario involving unzipping of chemical bonds is quite different from the way metals fracture. In metallic systems a crack may emit dislocations, and cavities may form in the damage zone surrounding the crack tip.

About a decade ago, we performed molecular dynamics (MD) simulations of fracture in a pre-cracked sample of amorphous silica (a-SiO_2) subjected to mode-I loading. The simulations revealed damage nucleation in the form of nanometre scale cavities in front of the pre-crack tip. On increasing the load, we observed growth and coalescence of nanocavities, crack extension and merging of damage cavities with the advancing crack front causing failure. These results raised a serious question: are the observed damage and failure mechanisms in a-SiO_2 caused by high strain rate deformation in the MD simulation or will they also manifest themselves in quasi-static fracture?

In 2003, Bouchaud and co-workers provided a definitive answer to this question in a paper entitled 'Glass breaks like metal, but at the nanometer scale' [2]. In their stress corrosion cracking (SCC) experiment, they observed damage nanocavities around the crack in silica glass with an atomic force microscope (AFM). Just as in the dynamic fracture simulations, the AFM experiment revealed growth and coalescence not only among damage nanocavities but also between the crack front and nanocavities.

In this review, we describe two additional MD simulations that reveal atomistic mechanisms of (1) nanovoid growth and the interaction and coalescence of nanovoids in a-SiO_2 under tensile loading and (2) growth and healing of cracks in silica glass under multiaxial compression. In section 2, we describe the parallel MD approach used to perform these multimillion-to-billion atom MD simulations. Section 2 also contains a description of the interatomic potential, and its validation through comparison with experiments and first-principles calculations. In section 3 we present results of billion-atom MD simulations of interaction and coalescence among nanovoids in a-SiO_2 under hydrostatic tension, followed by multimillion-atom simulations of wing crack formation, growth and healing in a-SiO_2. Section 4 provides an overview of the work in progress, which is focused on two sets of simulations: (1) multimillion-atom MD

 © 2009 IOP Publishing Ltd Printed in the UK

simulations over microsecond time scales to study the effect of strain rate on deformation and fracture in a-SiO_2 and (2) hybrid quantum, classical MD and continuum simulations of SCC in silica glass.

2. Parallel MD simulations

2.1. Interatomic potential

MD simulation approach provides the positions and velocities of an ensemble of atoms through the solution of Newton's equations of motion. This information is used to calculate structural, thermodynamic, mechanical and dynamical properties [3–6]. The essential input needed to perform an MD simulation is the potential through which atoms interact. The interatomic potential for silica consists of two-body and three-body terms [7]. The two-body potential includes steric repulsion due to the Pauli exclusion principle, screened Coulomb interaction arising from charge transfer between silicon and oxygen and charge-dipole interaction due to atomic polarizibilities:

$$V_{ij}^{(2)}(r) = \frac{A\,(\sigma_i+\sigma_i)^{\eta_{ij}}}{r^{\eta_{ij}}} + \frac{Z_i Z_j}{r} e^{-r/r_{1s}} - \frac{\left(\alpha_i Z_j^2 + \alpha_j Z_i^2\right)}{2r^4} e^{-r/r_{4s}}. \quad (1)$$

The three-body potential consists of bond-stretching and bond-bending covalent interactions:

$$V_{jik}^{(3)}\left(r_{ij}, r_{ik}\right) = B_{jik} \exp\left(\frac{\gamma}{r_{ij}-r_0} + \frac{\gamma}{r_{ik}-r_0}\right) \times \left(\cos\theta_{jik} - \cos\bar{\theta}_{jik}\right)^2 \Theta\left(r_0 - r_{ij}\right)\Theta\left(r_0 - r_{ik}\right). \quad (2)$$

The interaction potential is validated by comparing the MD simulation results with measurements of structural correlations, elastic moduli and phonon density of states of a-SiO_2. Amorphous silica is generated by the melt-quench method [8]. Starting with an atomic configuration of β-cristobalite, the system is heated to 3000 K, which is well over the melting temperature. This molten system is thermalized and cooled to room temperature. The system is well equilibrated at various intermediate temperatures and also at room temperature.

Figure 1(*a*) shows the comparison between neutron scattering measurements and MD calculation of the static structure factor, $S(q)$ [9]. Figure 1(*b*) shows experimental and MD results for the radial distribution function $T(r) = r^2 g(r)$, where $g(r)$ is the pair-distribution function. The simulation results for $S(q)$ and $T(r)$ are in excellent agreement with experiments [10, 11]. The agreement between MD and experimental measurements of $T(r)$ is especially significant because this function is more sensitive to medium-range correlations in silica glass than $g(r)$. The differences between experimental and MD results for $T(r)$ is less than 4% over the entire range of distances.

MD simulations provide a detailed picture of connectivity of atoms in a-SiO_2. Figure 2 is a snapshot of an a-SiO_2 network configuration at room temperature. In this network, each Si atom is bonded with 4 O atoms in the form of a SiO_4 tetrahedron and each O atom connects a pair of these tetrahedra in a corner-sharing configuration. The Si–O bonds in corner-sharing tetrahedra form –Si–O–Si–O– rings of various sizes with the ring distribution peaking at 6-membered rings, i.e. 6 Si–O pairs connected in a ring configuration.

We have also calculated the elastic moduli and fracture toughness to assess the validity of our interatomic potential in describing the mechanical properties of a-SiO_2. Table 1 shows a comparison between the MD results and experimental values of elastic moduli in a-SiO_2 [12]. The MD results are in reasonable accord with experiments—the deviations are less than 10%. The fracture toughness K_{1c} calculated with MD is 1 MPa $m^{1/2}$, and the experimental values range between 0.8 and 1.2 MPa $m^{1/2}$ [13–15].

First-principles quantum mechanical (QM) calculations based on density functional theory (DFT) further validate our interatomic potential for silica. We prepared a 192-atom a-SiO_2 system with MD simulation and relaxed it with the DFT [16, 17] method using a plane-wave pseudopotentials for the electron–ion interactions [18] and a parameter-independent generalized gradient approximation for the electron–electron exchange-correlation interactions [19]. The excellent agreement between DFT and MD simulations with regard to the network topology and short- and medium-range correlations further confirms the high quality of the interatomic potential for SiO_2. The DFT calculations also show that the forces on Si and O atoms deviate less than 4.5% and 6%, respectively, from the MD simulation for the same a-SiO_2 configuration.

2.2. Microcanonical, constant-temperature and constant-pressure ensembles

The most commonly used ensemble for MD simulations is the microcanonical ensemble, in which the total number of atoms N, the energy E and the system volume V are kept constant. Periodic boundary conditions (PBCs) are applied to minimize surface effects. In MD, the equations of motion,

$$\dot{r}_i = \frac{\partial H}{\partial p_i}, \qquad \dot{p}_i = -\frac{\partial H}{\partial r_i}, \quad (3)$$

are integrated in time. In equation (3), H is the Hamiltonian of the system:

$$H = \sum_{i=1}^{N} \frac{p_i^2}{2m_i} + \phi\left(\{r_i\}\right). \quad (4)$$

Nosé has developed a canonical ensemble MD method (constant N, V, T) by coupling the system to a thermostat, which is modelled with an additional degree of freedom

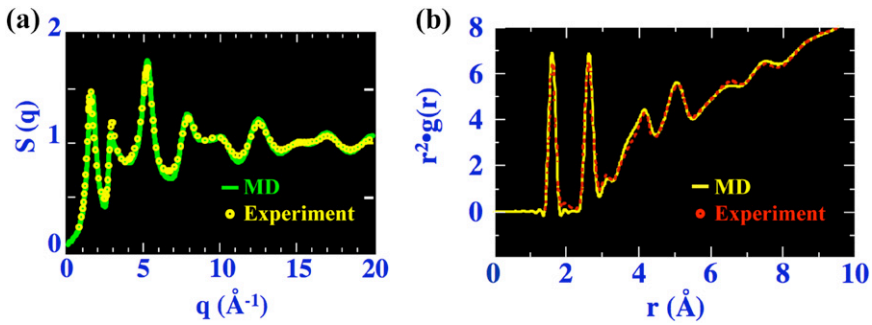

Figure 1. Comparison between MD simulation and experimental results for static structure factor and radial distribution function $T(r) = r^2 g(r)$.

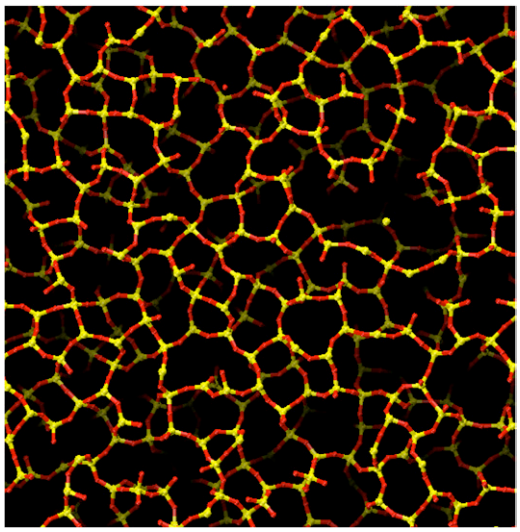

Figure 2. Snapshot of Si–O bond network in a-SiO_2. Yellow and red spheres represent silicon and oxygen atoms, respectively.

Table 1. Comparison between the MD and experimental data for elastic moduli of a-SiO_2.

Bulk Properties of a-SiO_2		
	MD	Experiment
C_{11} (GPa)	75.9	76.52
C_{12} (GPa)	20.9	18.78
C_{44} (GPa)	27.5	28.7

in the Hamiltonian:

$$H = \sum_{i=1}^{N} \frac{p_i^2}{2m_i s^2} + \phi\left(\{r_i\}\right) + \frac{p_s^2}{2Q} + N_f k_B T_{ext} \ln(s). \quad (5)$$

The first and second terms are the kinetic and potential energies of the physical system and the third and fourth terms represent those of the thermostat. k_B is the Boltzmann constant; s, p_s and Q are the coordinate, momentum and effective 'mass' of the thermostat, respectively. In Nosé dynamics, the time step fluctuates due to the time evolution of the scaling factor s. The real time and the so-called *virtual time* are related by $dt' = dt/s$. Hoover has modified Nosé dynamics to avoid the virtual time problem. The modified formulation, called Nosé–Hoover dynamics, is widely used to control temperature.

Martyna *et al* have extended Nosé–Hoover dynamics by introducing a layer of thermostats in the system. The Hamiltonian of a Nosé–Hoover chain with M linked thermostats is given as

$$H = \sum_{i=1}^{N} \frac{p_i^2}{2m_i} + V\left(\{r_i\}\right) + \sum_{i=1}^{M} \frac{p_{s_i}^2}{2Q_i} + N k_B T_{ext} s_1 + \sum_{i=2}^{M} k_B T_{s_i}, \quad (6)$$

and the equations of motion are

$$\boldsymbol{q}_i = \frac{\boldsymbol{p}_i}{m_i}, \quad (7)$$

$$\dot{\boldsymbol{p}}_i = -\nabla_{r_i}\phi\left(\{r_i\}\right) - \boldsymbol{p}_i \frac{p_{s_1}}{Q_1}, \quad (8)$$

$$\dot{s}_i = \frac{p_{s_i}}{Q_i}, \quad (9)$$

$$\dot{p}_{s_1} = \left[\sum_{i=1}^{N} \frac{p_i^2}{m_i} - N k_B T_{ext}\right] - p_{s_1} \frac{p_{s_2}}{Q_2}, \quad (10)$$

$$\dot{p}_{s_j} = \left[\frac{p_{s_{j-1}}^2}{Q_{j-1}} - k_B T_{ext}\right] - p_{s_j} \frac{p_{s_{j+1}}}{Q_{j+1}}, \quad (11)$$

$$\dot{p}_{s_M} = \frac{p_{s_{M-1}}^2}{Q_{M-1}} - k_B T_{ext}. \quad (12)$$

The choice of the effective masses of thermostats depends solely on the system of interest. They are taken to be

$$Q_{s_1} = \frac{3N k_B T_{ext}}{\omega_s^2}, \qquad Q_{s_i} = \frac{k_B T_{ext}}{\omega_s^2}, \quad (13)$$

where ω_s is the intrinsic thermal frequency of the system.

Andersen has developed a method to incorporate external pressure (barostat) to study isotropic changes in volume. In Andersen's dynamics, the volume of a system becomes a dynamic variable and the atomic positions are normalized by $V^{1/3}$, where V is the system volume. Parrinello and Rahman extended Andersen's dynamics to study structural phase transformation by including shape changes in the MD box system. A 3×3 matrix, the so-called H-matrix, spanned by three lattice vectors $(\boldsymbol{h}_1, \boldsymbol{h}_2, \boldsymbol{h}_3)$, describes the dimensions and shape of the MD box. The H-matrix becomes a dynamic variable, relating atomic coordinates $\boldsymbol{r}_i = (r_{ix}, r_{iy}, r_{iz})$ to scaled coordinates $\boldsymbol{s}_i = (s_{ix}, s_{iy}, s_{iz})$:

$$\boldsymbol{r}_i = s_{i1}\boldsymbol{h}_1 + s_{i2}\boldsymbol{h}_2 + s_{i3}\boldsymbol{h}_3 = \boldsymbol{H}\boldsymbol{s}_i, \quad (14)$$

where

$$\boldsymbol{H} = \begin{pmatrix} h_{1x} & h_{2x} & h_{3x} \\ h_{1y} & h_{2y} & h_{3y} \\ h_{1z} & h_{2z} & h_{3z} \end{pmatrix}. \tag{15}$$

The volume of the system V is obtained from $V = \det(\boldsymbol{H})$.

The MD simulations are also performed at constant pressure and constant temperature in the (NPT) ensemble. In this isothermal–isobaric ensemble, the Hamiltonian is

$$H = \sum_{i=1}^{N} \frac{p_i^2}{2m_i} + \phi\left(\{\vec{q}\}, V\right) + \frac{p_s^2}{2Q} + \frac{p_\varepsilon^2}{2W} + (3N+1)k_{\mathrm{B}}T_{\mathrm{req}}\ \ln(s) + P_{\mathrm{ext}}V, \tag{16}$$

where, s, p_s and Q are the same as in the Nosé–Hoover dynamics; p_{e} and W are the momentum and effective mass of the barostat, respectively; T_{req} is the thermostat temperature and P_{ext} is the barostat pressure. The equations of motion are

$$\dot{\boldsymbol{r}}_i = \frac{\boldsymbol{p}_i}{m_i} + \frac{p_\varepsilon}{W}\boldsymbol{r}_i, \tag{17}$$

$$\dot{\boldsymbol{p}}_i = -\nabla_{r_i}\phi\left(\{\boldsymbol{r}_i\}\right) - \left(1 + \frac{d}{3N}\right)\frac{p_\varepsilon}{W}\boldsymbol{p}_i - \frac{p_{s_1}}{Q_1}\boldsymbol{p}_i, \tag{18}$$

$$\dot{s} = \frac{p_s}{Q}, \tag{19}$$

$$\dot{p}_s = \sum_{i=1}^{N}\frac{p_i^2}{m_i} + \frac{p_\varepsilon^2}{W} - (3N+1)k_{\mathrm{B}}T_{\mathrm{ext}}, \tag{20}$$

$$\dot{V} = \frac{dVp_\varepsilon}{W}, \tag{21}$$

$$\dot{p}_\varepsilon = dV\left(P_{\mathrm{in}} - P_{\mathrm{ext}}\right) + \frac{d}{3N}\sum_{i=1}^{N}\frac{p_i^2}{m_i} - \frac{p_s}{Q}p_\varepsilon. \tag{22}$$

The internal pressure P_{in} is defined as

$$P_{\mathrm{in}} = \frac{1}{dV}\left[\sum_{i=1}^{N}\frac{p_i^2}{m_i} + \sum_{i=1}^{N}\boldsymbol{r}_i\cdot\nabla_{r_i}\phi\left(\{\boldsymbol{r}_i\}, V\right) - (dV)\frac{\partial\phi\left(\{\boldsymbol{r}_i\}, V\right)}{\partial V}\right], \tag{23}$$

where d denotes the spatial dimensions of the systems. The mass of the barostat is chosen to be

$$W = \frac{(3N+d)k_{\mathrm{B}}T_{\mathrm{ext}}}{\omega_{\mathrm{b}}^2}, \tag{24}$$

where ω_{b} is the intrinsic frequency at which the volume of the MD box fluctuates.

2.3. Integration algorithms

Numerous integration algorithms have been proposed, and each has advantages and disadvantages, e.g. numerical accuracy, algorithmic simplicity or memory demand. The most commonly used algorithm is the velocity-Verlet algorithm, which is symplectic (phase-space conservation) and time-reversible.

Tuckerman *et al* have developed a multiple time step (MTS) integration algorithm, called reversible reference system propagator algorithm (RESPA) [20]. Usually several regimes requiring distinct time resolution exist for one interatomic potential. Stiffer interactions with a steeper slope need to be updated more frequently, while it is unnecessary to frequently update softer interactions. The idea behind the MTS method is to partition the potential energy function into several parts according to their characteristic time scale, and perform time integration with appropriate time resolution. Due to its simplicity, stability and flexibility in algorithm design, RESPA is a very powerful integration scheme.

Derivation of the velocity-Verlet algorithm based on the RESPA is as follows. Let $\Gamma(t)$ be a state $\{\boldsymbol{r}_i(t), \boldsymbol{p}_i(t)\}$ in the phase space at time t. According to Liouville's theorem, the phase space volume does not change with time. The time variation of the state Γ can be expressed as

$$i\frac{\partial\Gamma}{\partial t} = -L\Gamma, \tag{25}$$

where L, the Liouville operator, is defined as

$$i\Gamma = \{..., H\}. \tag{26}$$

In equation (26), $\{\ldots,\ldots\}$ is the Poisson bracket. With the Hamiltonian given in equation (3), the Liouville operator becomes

$$iL = \sum_{j=1}^{N}\left[\boldsymbol{v}_j\frac{\partial}{\partial\boldsymbol{r}_j} + \boldsymbol{f}_j\frac{\partial}{\partial\boldsymbol{p}_j}\right]. \tag{27}$$

The formal solution of equation (26) may be written as

$$\Gamma(t) = \mathrm{e}^{iLt}\Gamma(0) \equiv U(t)\Gamma(0). \tag{28}$$

Here, $U(t)$ is a time evolution operator. According to the Trotter decomposition, the following relation holds for non-commutable operators:

$$\exp[\Delta t(L_1+L_2)] = \left\{\exp\left[\frac{\delta t}{2}L_1\right]\exp\left[\delta t L_2\right]\exp\left[\frac{\delta t}{2}L_1\right]\right\}^M + O\left(\frac{\Delta t^3}{M^2}\right), \tag{29}$$

where $\delta t = \Delta t/M$ and M is an integer. Let the operators L_1 and L_2 be

$$L_1 = \sum_{j=1}^{N}\boldsymbol{f}_j\frac{\partial}{\partial\boldsymbol{p}_j}, \qquad L_2 = \sum_{j=1}^{N}\boldsymbol{v}_j\frac{\partial}{\partial\boldsymbol{r}_j} \tag{30}$$

and $M = 1$. Substituting them into equations (29) and (30),

$$\begin{aligned}\Gamma(\mathrm{d}t) &= \mathrm{e}^{iL\mathrm{d}t}\Gamma(0)\\ &= \mathrm{e}^{iL_1\mathrm{d}t/2}\mathrm{e}^{iL_2\mathrm{d}t}\mathrm{e}^{iL_1\mathrm{d}t/2}\Gamma(0) + O(\mathrm{d}t^3)\\ &= \mathrm{e}^{(\mathrm{d}t/2)\sum_{j=1}^{N}\boldsymbol{f}_j\frac{\partial}{\partial\boldsymbol{p}_j}}\mathrm{e}^{\mathrm{d}t\sum_{j=1}^{N}\boldsymbol{v}_j\frac{\partial}{\partial\boldsymbol{r}_j}}\mathrm{e}^{(\mathrm{d}t/2)\sum_{j=1}^{N}\boldsymbol{f}_j\frac{\partial}{\partial\boldsymbol{p}_j}}\Gamma(0)\\ &\quad + O(\mathrm{d}t^3).\end{aligned} \tag{31}$$

When $\mathrm{d}t$ is small enough, equation (31) can be implemented as

$$\begin{aligned}&\Gamma(0): v_i \to v_i + \frac{f_i}{m_i}(\mathrm{d}t/2),\\ &\Gamma(\mathrm{d}t/2): r_i \to r_i + v_i\mathrm{d}t,\\ &\Gamma(\mathrm{d}t): v \to v + \frac{f_i}{m_i}(\mathrm{d}t/2).\end{aligned} \tag{32}$$

This is the velocity-Verlet algorithm.

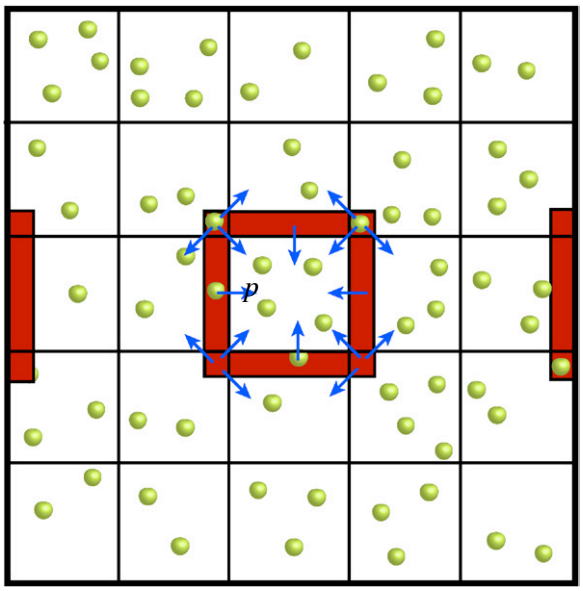

Figure 3. Schematic of a two-dimensional spatial decomposition. To calculate force, the internode communication is required to cache atomic coordinates from neighbour domains. After updating atomic coordinates, atoms outside the resident domain are transferred via message passing.

2.4. Parallel MD algorithms

In an MD simulation, the force on an atom i is determined by the positions of neighbouring atoms within a finite interaction range. For this reason, spatial decomposition is commonly used to parallelize MD simulations [21]. Using the divide-and-conquer strategy, the spatial decomposition technique divides the simulation volume into $P = P_x \times P_y \times P_z$ sub-domains of equal volume, which are mapped onto processors in a parallel computer. Atom i at position $\boldsymbol{r}_i = (r_{ix}, r_{iy}, r_{iz})$ belongs to the spatial domain of processor p:

$$p = p_x P_y P_z + p_y P_z + p_z,$$

$$p_\alpha = \lfloor r_{i\alpha} P_\alpha / L_\alpha \rfloor, \tag{33}$$

where α denotes a Cartesian coordinate and L_α represent the lengths of the MD box. Information about atomic positions and velocities and atom types within the spatial sub-domain is assigned to the processor p. The domain of every processor is extended to access positions of atoms within a cutoff distance from the boundaries of neighbouring processors, and the subsequent force calculation is then local to the processor. Figure 3 shows the 'extended' domain (red) of a processor p. Atom information near the boundary of the neighbouring processors is cached into p.

To minimize the communication time, each processor is assigned a sufficiently large number of atoms so that caching of atoms from neighbouring processors is negligible compared with the local computation time. The internode communication involves sending and receiving data from 26 neighbouring domains. In the 'caching' process, attributes of the skin-layer atoms are sent to left, right, top, bottom, back and front nearest neighbour processors consecutively. When atoms move out of the domain of a processor after the position updates, data attributes of those atoms are transferred to the neighbouring processor. The Message passing interface (MPI) library [22] is used to communicate between processors.

Linked-cell list and neighbour-list methods are also used in our MD simulations. The linked-cell list method decomposes the subsystem into smaller cells whose dimensions are slightly larger than the potential cutoff, $r_c + \delta$, where δ is the 'skin'. To calculate the force on an atom, one simply needs to calculate the contributions from atoms in the same cell and from atoms in the 13 nearest neighbour cells (with the use of Newton's third law).

2.5. Performance of parallel MD algorithms

Shared-memory and distributed-memory systems are available for parallel computations. In a shared-memory system, more than one processor can access the same memory. The size of the memory assigned to the processor is limited. Multi-processor computers, where each processor runs tasks independently of other processors, belong to this category. Processors in one node have the advantage of fast data communication speed.

In a distributed-memory machine, each processor has its own private memory and inter-processor communication is done via the interconnect. The data communication scheme in such a machine is implemented by the end user using a parallel programming library, such as message passing interface (MPI). This architecture has the scalability advantage. A Beowulf cluster is an example of a distributed-memory system.

A hybrid distributed-shared memory system is a combination of the above two architectures. It consists of linked computing nodes, where each node is a multi-processor machine. The 6,120-processor Linux cluster at the High Performance Computing Center (HPCC) at USC and the 2,048-processor Linux clusters in our Collaboratory for Advanced Computing and Simulations (CACS) use this architecture.

The efficiency, E, is an important measure of parallel algorithm. It is defined as

$$E = \frac{S_\mathrm{p}}{p} = \frac{W_\mathrm{p} T(W, 1)}{P W_1 T(W_\mathrm{p}, p)}. \tag{34}$$

S_p is the speedup of the program on p processors:

$$S_\mathrm{p} = \frac{S(W, p)}{S(W, 1)} = \frac{W_\mathrm{p} T(W, 1)}{W_1 T(W, p)}, \tag{35}$$

where $T(W, 1)$ and $T(W, p)$ are the total execution times on 1 and p processors, respectively. In an ideal situation, a simulation on p processors should be p times faster than on a single processor with the same workload. Therefore, an ideal algorithm has an efficiency of 1.

Figure 4 shows benchmark results for isogranular (constant amount of computation per processor) scalability on 212,992-processor BlueGene/L at the Lawrence Livermore National Laboratory and 131,072-processor BlueGene/P at the Argonne National Laboratory. In both cases the parallel efficiency exceeds 0.97, showing excellent parallel scalability of the divide-and-conquer scheme for MD simulations.

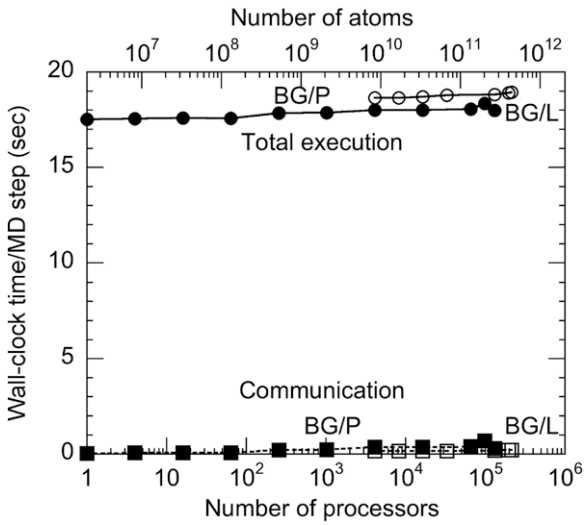

Figure 4. Isognranular scalability of parallel MD algorithm on BlueGene/L&P. The number of atoms per processor N/P is 2 044 416.

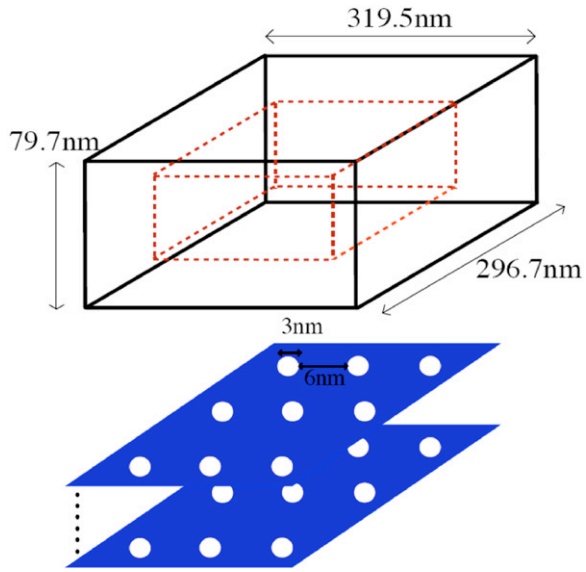

Figure 5. Schematic of the setup for the 500 void simulations. Red-dotted lines indicate the region in which voids are initially located either in a regular or random array.

3. Results

3.1. Interaction and coalescence of voids and nanoductility in silica glass

We have performed billion-atom MD simulations to study the effect of dilatational strain on an ensemble of spherical nanovoids in silica glass [6]. Two sets of initial configurations of voids are considered; (i) voids in a regular configuration and (ii) random, non-overlapping distribution of voids. The void diameter is 3 nm and the minimum void–void separation (centre-to-centre) in both systems is 6 nm. In total, 500 voids are placed at the centre of the specimen, about 100 nm from the boundaries in the x and y directions and 60 nm from the boundaries in the z direction (the area enclosed by the red-dotted line in figure 5). The system size is $319.5 \times 296.7 \times 179.7\,\text{nm}^3$.

To examine the growth of and the interaction between a pair of voids, we have also performed simulations of 1 million and 15 million atoms with various void sizes and initial inter-void separations. The dimension of the 1 million-atom system is $(25.6\,\text{nm})^3$ and of the 15 million atoms system $(62.8\,\text{nm})^3$. We apply PBCs in the x, y and z directions. The simulations are performed at constant strain rates of 10^8 or $10^9\,\text{s}^{-1}$. The strain is applied using the Parrinello–Rahman approach.

All silica glass specimens were prepared by the melt-quench method and well thermalized at room temperature. After creating spherical voids by removing atoms, the conjugate gradient method is used to relax the system. Then the systems are gradually heated to room temperature and thermalized again. The total simulation times are 550 ps for the 1 million-atom and 15 million-atom systems and 120 ps for the billion-atom systems.

The snapshot in figure 6(a) shows the growth of two voids in a million-atom system. The strain rate is $10^8\,\text{s}^{-1}$, the initial void diameter is 3 nm and the initial centre-to-centre distance between the voids is 6 nm. Up to a strain of $\varepsilon = 4\%$, the voids grow independently as their diameters increase from 3 to 3.5 nm. Further increase in the strain nucleates damage cavities in the inter-void ligament region. To distinguish the effect of inter-void interaction from individual void growth, we have performed million-atom simulations for a single void under exactly the same conditions. Figure 6(b) shows the ratio of the porosity per void in the two-void system, ϕ_2 to the porosity of the single-void system, ϕ_1, at small strains. Above $\varepsilon = 7\%$, the ratio ϕ_2/ϕ_1 is large and nanocracks appear on the void surface in the two voids system. In addition, damage nanocavities nucleate and grow in the inter-void ligament region. Finally at $\varepsilon = 8\%$, the ligament fractures when cavities coalesce. We find that the relation between inter-void ligament distance and initial void size in silica glass agrees qualitatively with Brown–Embury criterion for ductile materials.

Significant structural changes occur in the ligament region due to void–void interaction prior to ligament fracture. Figures 6(c) and (d) show Si–O pair correlation function, $g_{\text{Si–O}}(r)$, and Si–O–Si bond angle distribution, $P_{\text{Si–O–Si}}(\theta)$, before and after the strain is applied. At $\varepsilon = 8\%$, the height of the first peak in $g_{\text{Si–O}}(r)$ decreases significantly from the unstrained case. This is caused by Si–O bond breaking and a decrease in the atomic coordination. The height of the second peak in $g_{\text{Si–O}}(r)$ also drops, indicating structural changes in –Si–O–Si–O–Si– rings.

Our simulations reveal a novel damage cavity nucleation mechanism via strain-enhanced defect transport; see figures 7(a)–(c). In silica glass, each silicon atom has four nearest neighbour oxygen atoms forming a SiO_4 tetrahedron and oxygen atoms are bonded with two silicon atoms connecting SiO_4 tetrahedra at the corners. This structure provides short-to-middle range order consisting of nanometre size –Si–O–Si–O–Si–O– rings. Figure 7(a) displays a snapshot of the unstrained Si–O bond network of Si (yellow) and O (red) atoms in the inter-void ligament. The blue, green and grey shaded areas highlight regions enclosed by a 7-, 6- and 5-membered –O–Si–O–Si– rings, respectively. The

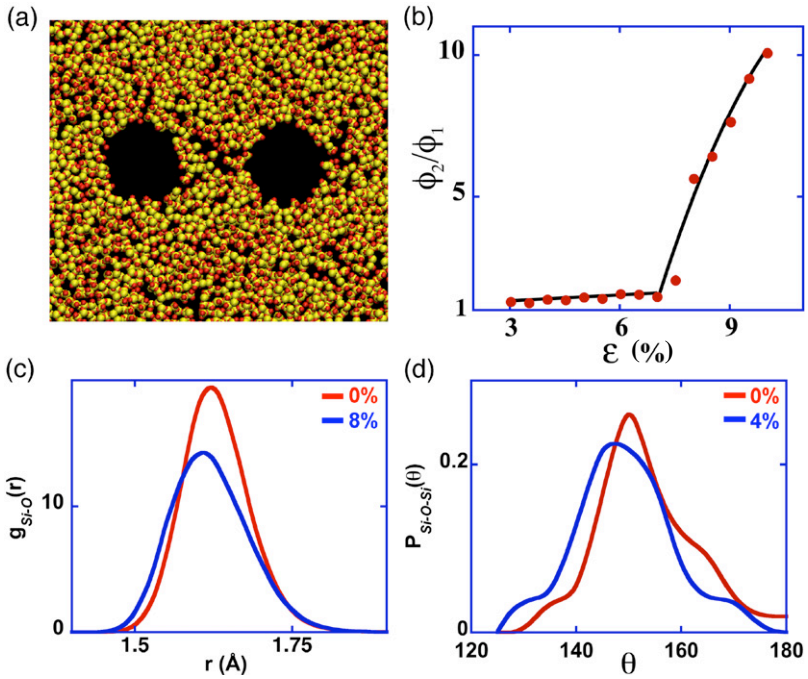

Figure 6. (*a*) Snapshot of voids and nanocavities at a strain rate of $10^8\ s^{-1}$. (*b*) Strain dependence of the average porosity per void in the two-void system, ϕ_2, relative to the porosity of the single-void system ϕ_1. (*c*) Si–O pair distribution functions and (d) Si–O–Si bond angle distributions in the middle of the inter-void ligament in the unstrained and strained systems.

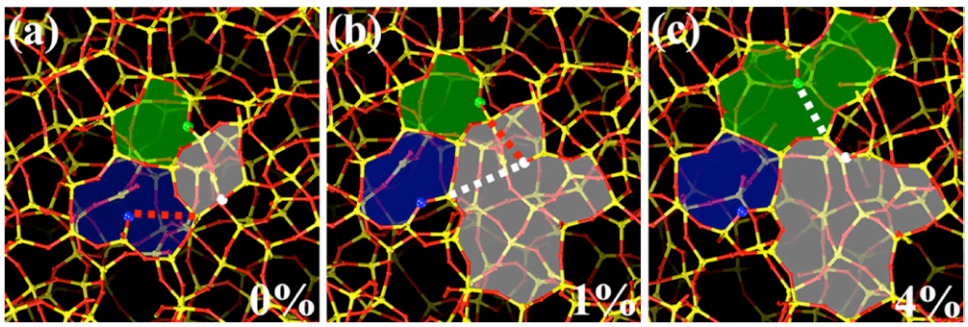

Figure 7. Bond switching mechanism involving non-bridging O atoms is shown in (*a*) and (*b*) by red and white dashed lines between blue and white atoms. In (*c*), the white dashed line indicates bond switching between white and green O atoms.

blue sphere shows an initially undercoordinated O (only one Si as a neighbour atom) that belongs to the 7-memberd ring. The green and white spheres are O atoms with normal coordination (2) at the beginning. Later on, these atoms play a pivotal role in the nucleation and growth of a nanocavity. Increasing the strain to 1%, the undercoordinated O (blue) acquires normal coordination by bonding with a Si that was one of the neighbours of O (white) (see figure 7)). This O (white) atom ruptures a bond with the Si and becomes undercoordinated. As a result, the 5-membered ring (grey) becomes a 12-membered ring (increasing the volume of open space) and the 7-membered ring (blue) shrinks to a 5-membered ring. Similarly at a strain of 4%, one of the Si atoms connected with an O (green) breaks its bond and forms a new bond with O (white) (see figure 7(*c*)). Bond switching from Si–O (green) to Si–O (white) results in 11-membered (grey) and 10-membered (green) rings. Due to two consecutive bond switching events, an undercoordinated O effectively migrates. The transport of non-bridging O is driven by stress gradients. This mechanism nucleates nanometre size voids. We have observed the same mechanisms for the nucleation and growth of damage nanocavities and inter-void ligament failure in the 15 million-atom SiO_2 glass at a strain rate of $10^9\ s^{-1}$.

Figures 8(*a*)–(*f*) show the growth and coalescence of voids when they are arranged in a regular array or distributed randomly. These are the results of billion-atom simulations in which the systems are subjected to a dilatational strain rate of $10^9\ s^{-1}$. In the case of a regular array of voids (figures 8(*a*)–(*c*)), sheets of nanocavities nucleate in inter-void ligaments and small cracks appear on void surfaces at $\varepsilon = 4.5\%$. Nanocavity nucleation begins in ligaments bridging the nearest and second nearest neighbour voids (diagonal ligaments). The voids and nanocavities in ligaments continue to grow until the strain reaches 9%, and then a number of ligaments fracture at the corner boundaries of the regular array (figure 8(*a*)). Figure 8(*b*) shows coalescence of multiple voids at slightly larger strain $\varepsilon = 10.5\%$. These fractures of inter-void ligaments locally release strains, and as a result

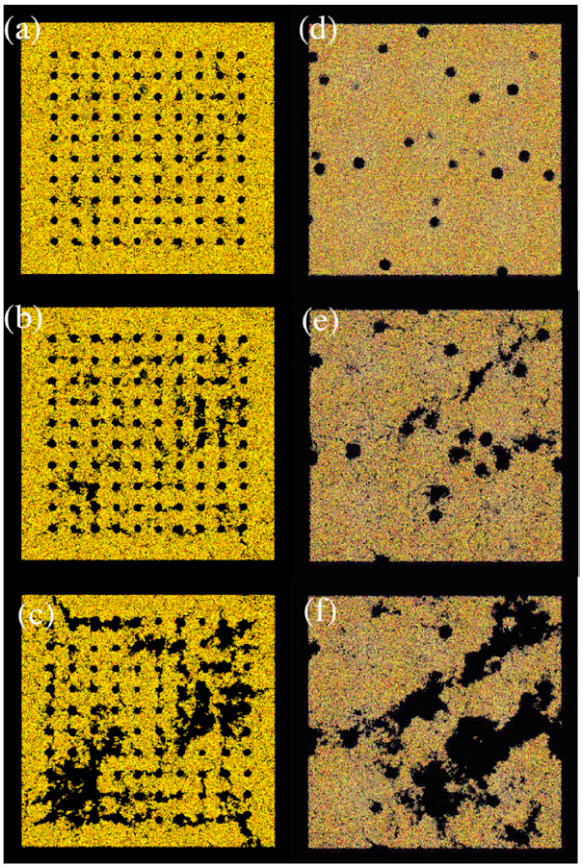

Figure 8. Growth of voids and void coalescence in a billion-atom system under dilatational strain. The strain rate is $10^9\ s^{-1}$. Panels (a)–(c) show damage in a regular array of voids; and panels (d)–(f) show damage in a random distribution of voids. For clarity, a slice of the entire system is shown; (a) crack nucleation on void surfaces at $\varepsilon = 9\%$; (b) and (c) show void coalescence and inter-void ligament failure at $\varepsilon = 10.5\%$ and $\varepsilon = 12\%$, respectively. (d) a snapshot of randomly distributed voids; (e) onset of void coalescence and ligament failure at $\varepsilon = 8\%$ and (f) formation of a few large cavities at $\varepsilon = 10\%$.

voids shrink and cracks on the void surfaces begin to heal. At $\varepsilon = 12\%$, many voids coalesce into a few large cavities (figure 8(c)). Figures 8(d)–(f) show snapshots of randomly distributed voids at $\varepsilon = 0\%$, 7% and 10%, respectively. Overall the void growth and coalescence are similar to the case of a regular array of voids. As the strain increases, the voids first grow independently without any significant damage around them. However, surface cracking and void coalescence start at a strain of ∼8%. The void–void interaction and eventual coalescence are again mediated by the nucleation and growth of nanocavities in inter-void ligament regions.

We have performed percolation analysis to investigate the porosity as a function of the applied strain. Figures 9(a)–(c) show the spatial distribution of connected empty volumes in the randomly distributed voids at $\varepsilon = 5\%$, 8% and 10%, respectively. At small strain, the size of each void is nearly identical. Many voids merge into a few large cavities at $\varepsilon = 8\%$, where a sharp kink appears in the porosity–strain curve (see figure 9(d)). Figure 9(c) shows a mosaic of cracks resulting from the percolation of voids through the system at a strain of 10%.

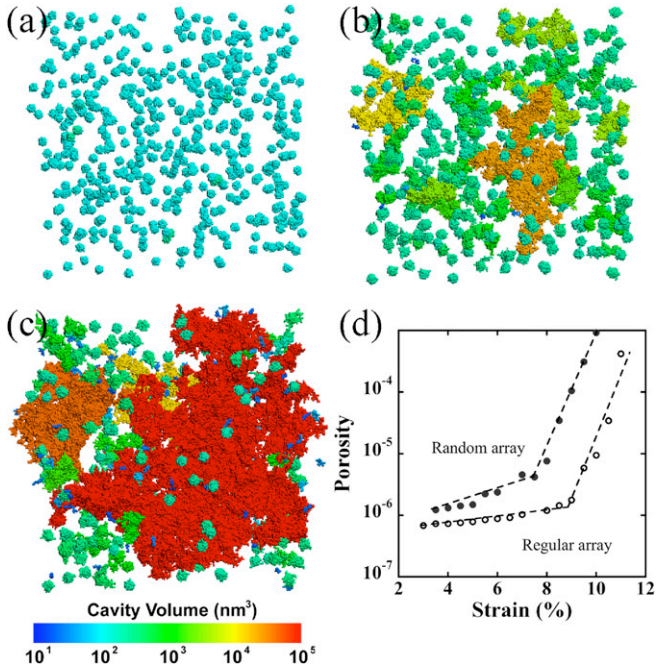

Figure 9. (a)–(c) Volumes of coalesced cavities in the random void array system at $\varepsilon = 5\%$, 8% and 10%, respectively. (d) Porosities versus strain in billion-atom systems containing 500 identical voids distributed regularly and randomly.

3.2. Dynamics of wing cracks and nanoscale damage in silica glass

Figure 10(a) schematically shows the wing-crack simulation setup. We first prepared a bulk a-SiO_2 system with dimensions $120 \times 120 \times 15\,(nm^3)$ starting with an ideal β-cristobalite crystal and using the melt-quench method. Next, PBCs are removed in the x and y directions and a 40 nm long pre-crack is inserted. Subsequently, the system is relaxed and quenched to 0 K. After applying the conjugate gradient method, the system is thermalized at 10 K and confined by purely repulsive walls. A rigid indenter applies an impulse load to the upper half of the sample, but the lower half is not subjected to an external load. The indenter speed is kept constant, either at $150\ m\ s^{-1}$ or $375\ m\ s^{-1}$, which are 5% and 12.5% of the Rayleigh wave speed V_R ($\sim 3000\ m\ s^{-1}$) in silica glass, respectively.

The crack morphology is examined using percolation analysis (see figure 10(b)). We partition the simulation system into small voxels, and each voxel is assigned a flag indicating that the voxel is 'filled' if it contains an atom or otherwise 'empty'. The voxel dimensions are $(4.5\ Å)^3$, which is the second nearest neighbour Si–O distance. Breadth-first search algorithm gives the shape of the crack for any given atomic configuration. Any set of connected 'empty' is considered a damage cavity if those voxels are disconnected from the pre-crack.

In addition to the analyses of crack and void morphologies, we monitor stress distributions around the pre-crack [5]. Atomistic-level stresses for distances greater than 10 nm from the pre-crack tip show good agreement with mode II stress distributions in linear elastic fracture mechanics (LEFM). However, the stress distributions in the MD simulation differ

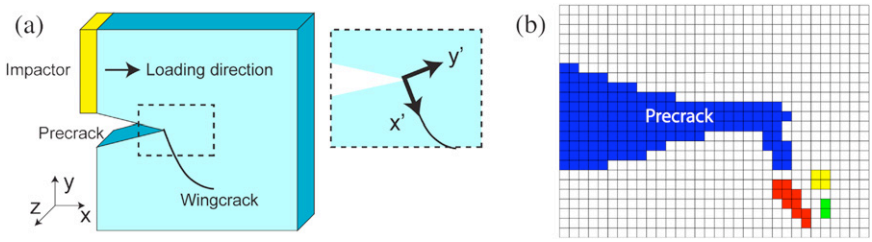

Figure 10. Setup of the wing crack simulation. A yellow rectangular plate represents a rigid indenter and the blue parallelepiped is the pre-cracked silica glass. The pre-crack length is 40 nm. The silica sample is confined in the x and y directions and PBC is applied in the z direction. Inset shows a close-up view of the pre-crack tip and resolved coordinates x' and y' used for stress calculation. (b) Schematic of the crack-morphology analysis. The system is divided into small cells and connected cells are identified by breadth-first search. The blue cells represent the pre-crack and cracks emanating from there. Red, yellow and green cells indicate damage nanocavities.

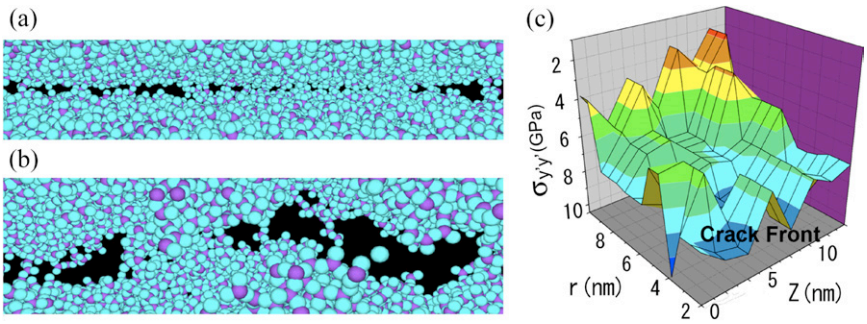

Figure 11. (a) Snapshot of the pre-crack tip showing silicon (purple) and oxygen (light blue) atoms, and the nucleation of nanocavities (black) due to frictional sliding of the crack surfaces; (b) atomistic view of kinks formed by nanocavities (black); (c) resolved tensile stress $\sigma_{y'y'}$, along the crack front (z) as a function of the distance, x', from the pre-crack tip. The resolved coordinates are obtained by rotating x and y axes 70° around the z axis. The impact speed is $0.05v_R$, where v_R is the Rayleigh wave speed.

significantly from the LEFM results for distances less than 10 nm from the pre-crack tip because of the discrete nature of the material at such short distances.

When the compression wave generated by the indenter pushing the upper half of the silica specimen (above the pre-crack from left to right in figure 10(a)) reaches the pre-crack tip, the top surface of the pre-crack begins to slide relative to the bottom surface. This sliding motion nucleates damage nanocavities at the pre-crack tip. Figures 11(a)–(b) show atomic views of the nanocavity nucleations (black) and kinking of the crack. Figure 11(c) is a plot of the stress component $\sigma_{y'y'}$, which is perpendicular to the kink direction, x', of the pre-crack. The damage nanocavities grow and the crack bends 70° from the pre-crack in the direction of the maximum mode I tension. This MD result agrees well not only with the LEFM but also with macroscopic quasi-static and dynamic compression experiments on brittle materials.

MD simulations also reveal that nanocavities coalesce to form crack nanocolumns. Figure 12 shows the formation and growth of a wing crack at (a) 19 ps and (b) 21 ps after the load is applied. Nanocavities (red, yellow, orange, green and dark blue) grow around the pre-crack and merge into nanocolumns. A couple of picoseconds later, these nanocavities and nanocolums join to form a wing crack. Nanocavitation is observed in the tensile stress region ahead of the moving crack tip. After reaching a length of 9 nm, the wing crack encounters a compression wave reflected from the right end of the system (see figure 10(a)). This makes the wing crack recede in the next 7 ps at an average speed of 1300 m s^{-1}.

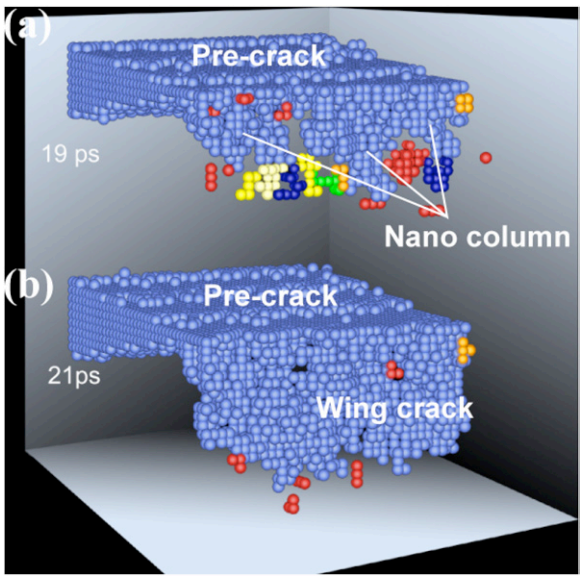

Figure 12. Wing crack formation and growth, and damage cavities (red, yellow, green, dark blue and orange).

We observe that the pre-crack grows when the wing crack is healing and vice-versa. During the first healing of the wing crack, the pre-crack length increases by 5 nm over 11 ps via nucleation and coalescence of nanocavities formed in front of the pre-crack. After that, the pre-crack starts receding and is partially healed while the wing crack reemerges and propagates at an average speed of 1500 m s^{-1}. Figure 13 shows

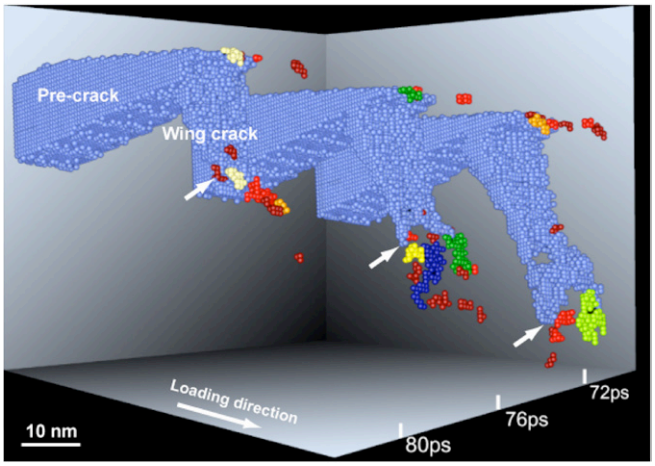

Figure 13. Second healing of the wing crack. (Right) Snapshot of the wing crack and pre-crack right before the wing crack recedes. The wing crack tip splits into two columns creating a few damage cavities (green and red) near the tip. (Middle) In the next 4 ps the wing crack recedes considerably and leaves damage cavities (red, yellow, green and blue) behind. (Left) Snapshot of the wing crack and cavities after healing. White arrows indicate positions of the wing crack tip.

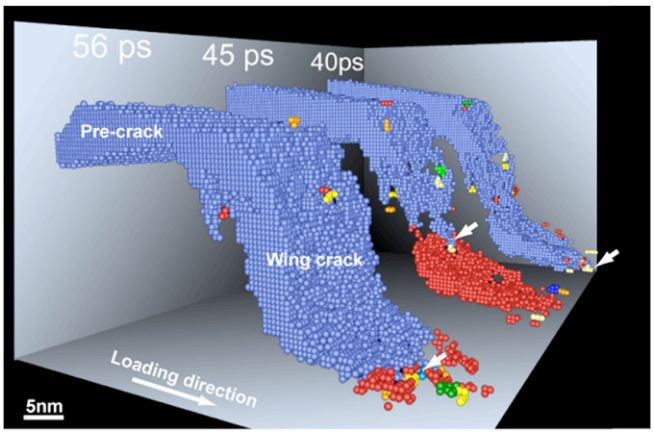

Figure 14. Snapshots of the wing crack and nanocavities at $0.125v_R$, where v_R is the Rayleigh wave speed in silica glass. (Right) snapshot shows the wing crack turned in the loading direction; (middle) a large cavity (red) splits off the wing crack; (left) after 4 ps the cavity merges with the wing crack. A secondary wing crack appears behind the main wing crack.

three snapshots of the wing crack during the second retreat at 72 ps (right), 76 ps (middle) and 80 ps (left), respectively. The right snapshot shows that after reaching a maximum length of 27 nm the wing crack encounters compression waves from the confining walls. Two large nanocativies (green and read) and a few small cavities appear ahead of the wing crack and around the pre-crack tip. The middle snapshot (at 76 ps) shows that the wing crack recedes significantly leaving behind large (blue and green) and small (red and yellow) nanocavities. The wing crack stops receding and leaves behind damage nanocativies (see the left snapshot at 80 ps). The average speed of the receding wing crack is about 800 m s^{-1} and the residual length of the wing crack is 13 nm. The wing crack propagates and retreats repeatedly, and this kind of 'initiation, growth and arrest' of wing cracks under lateral confinement have also been observed in dynamic compression experiments on a ceramic glass [23].

At the higher impact loading speed, $v_i = 0.125v_R$, we observe similar mechanisms for wing crack formation via the nucleation, growth and coalescence of nanocavities and nanocolumns. The pre-crack tip again kinks towards maximum mode I tension (70° around the z axis) and grows to a length of 21 nm over 17.5 ps. Over the next 10 ps, the wing crack propagates in the direction of maximum compression at one-third the speed of Rayleigh waves. This change in the direction of the wing crack propagation towards maximum compression is always observed in quasi-static and dynamic compression experiments.

We find significant differences in the healing of the wing crack and resulting damage nanocavities from those at the lower impact loading speed. In figure 14, the right snapshot (at 40 ps) shows the wing crack and nanocavities right after the crack reaches a maximum length of 31 nm. At 45 ps, the wing crack splits off and leaves behind a 20 nm long cavity (red) due to the arrival of compression wave reflected from the sidewalls. The crack continues to heal and the cavity rejoins the crack shortly after the passage of compression wave. A secondary wing crack nucleates and residual damage cavities remain ahead of the retreating crack (at 56 ps). On running the simulation longer, we again observe repeated growth-and-retreat sequence of the wing crack.

4. Work in progress

Currently we are investigating (1) the effect of strain rate in MD simulations on deformation and fracture in silica glass and (2) SCC of a-SiO_2 in the presence of water using a hybrid, multiscale approach. We are performing multimillion-atom simulations of damage evolution during crack propagation in silica glass over microsecond time scales. In this simulation, the strain rate is several orders of magnitude less than those in the simulations presented in sections 3.1 and 3.2.

SCC is a challenging simulation problem [24, 25]. To do meaningful SCC simulations, multiple size domains need to be considered and each of these domains requires a different computational approach. The domains need to be nested, as regions far from process zones do not need the detailed description necessary for accurate prediction near the crack tip.

Near the crack tip, QM simulations based on DFT are performed. Usually, the QM region is surrounded by an effective force field (EFF) MD. The QM/EFF boundary has been the subject of many studies over the last few years, and although this has resulted in several reasonably successful hybrid simulation schemes, a straightforward, material-independent communication strategy between these methods still remains elusive. The problem at the QM/EFF interface lies in the fact that the charge flow and bond breaking events at the QM electronic scale are difficult to translate into the regime of rigid bonding/fixed point charges usually employed at the EFF-level.

To facilitate a smooth transition between QM and EFF, it is necessary to insert a computational method that shares many

common features with both approaches. It must have the ability to dissociate and create chemical bonds and handle charge flow by employing a chemical-environment dependent charge model. Goddard and co-workers have developed the first-principles based reactive force fields (ReaxFF) [26] to interface QM and EFF-methods. ReaxFF studies have already been reported for a wide range of materials, including ceramics, metals and metal oxides.

Our effort to simulate SCC in silica glass builds upon our recent work on multiscale QM/MD/finite element (FE) simulations, including ReaxFF-MD studies of reactive materials. We have performed a hybrid MD/DFT simulation study of the reaction of water at a crack tip in silicon [27]. The simulation shows significant dependence of the reaction between H_2O molecules and the crack on the stress intensity factor.

We have also performed hybrid MD/FE simulation on a silicon/silicon-nitride nanopixel [28], which is commonly used in microelectronics. The hybrid approach involves MD simulation near the Si/Si_3N_4 interface and FE modelling deep into the Si substrate, thereby significantly increasing the accessible length scales and greatly reducing the computational cost. Displacement fields of the full MD and the hybrid MD/FE simulations are in excellent agreement with each other. The MD/FE results for residual stresses in the nanopixel are also in agreement with the full MD calculation.

Recently we have successfully demonstrated a tightly coupled, hybrid QM/MD simulation of SIMOX (separation by implanted oxygen) technique [29]. The simulation ran on six supercomputers in the US (National Center for Supercomputing Applications, Pittsburgh Supercomputing Center, University of Southern California) and Japan (Advanced Industrial Science and Technology, Tokyo Institute of Technology and University of Tokyo) using a reservation-based sustainable adaptive Grid supercomputing paradigm.

Our latest effort in hybrid simulation algorithms involves the development of an atomistic/continuum simulation scheme for solid–liquid interfaces. We have coupled MD with the mesoscopic lattice-Boltzmann (LB) method using the Schwartz alternating method, which iteratively finds a consistent solution in the atomistic and continuum domains by implicitly imposing flux continuity but without direct exchange of fluxes. In our implementation, PBC is not invoked but the density in the MD region is kept constant by applying a mean boundary force and by using specular walls and an efficient particle insertion scheme.

In the continuum domain, we use the LB method to solve a minimal form of the Boltzmann kinetic equation ignoring all details of molecular motion except those needed to recover hydrodynamic behaviour at the macroscopic scale. For hierarchical fluid flow simulations, we have developed an extensible LB computational framework for tera-to-petascale parallel/distributed platforms. The LB framework includes scalable algorithms and tools as well as capabilities for handling, analysing and visualizing petabyte simulation datasets. It allows collaborative construction and execution of complex, multi-component, computationally demanding hybrid numerical simulations of fluid flow. We have achieved scalability beyond 10^5 processors through linear-scaling algorithms and performance-optimization techniques. Recently, we have performed the LB simulations of fluid flow through a network of cracks in amorphous silica on a cluster of cell processors using PlayStation3 consoles [30, 31]; see figure 15.

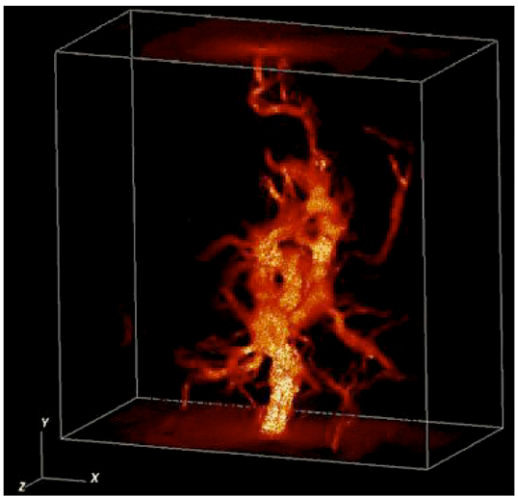

Figure 15. Snapshot of fluid flow in fractured silica performed on the PlayStation3 cluster. Here the magnitude of the fluid velocity is colour-coded.

Acknowledgments

The authors would like to thank Drs Elisabeth Bouchaud and Cindy Rountree for many useful discussions. This work was supported by a DOE-SciDAC grant. Simulations were performed on the 6,120-processor Linux cluster at the USC's Research Computing Facility and on the 2,048-processor Linux cluster at our Collaboratory for Advanced Computing and Simulations. Work performed by LHY was under the auspices of the US Department of Energy by Lawrence Livermore National Laboratory under Contract DE-AC52-07NA27344.

References

[1] Yip S 2005 *Handbook of Materials Modeling* (Dordrecht: Springer)
[2] Celarie F *et al* 2003 *Phys. Rev. Lett.* **90** 075504
[3] Campbell T *et al* 1999 *Phys. Rev. Lett.* **82** 4018
[4] Rountree C L *et al* 2002 *Annu. Rev. Mater. Res.* **32** 377
[5] Lu Z *et al* 2005 *Phys. Rev. Lett.* **95** 135501
[6] Chen Y C *et al* 2007 *Phys. Rev. Lett.* **99** 155506
[7] Vashishta P, Kalia R K, Nakano A, Li W and Ebbsjo I 1996 *Amorphous Insulators and Semiconductors* ed M F Thorpe and M I Mitkova (Dordrecht: Kluwer) p 151
[8] Vashishta P *et al* 1990 *Phys. Rev.* B **41** 12197
[9] Nakano A, Kalia R K and Vashishta P 1994 *J. Non-Cryst. Solids* **171** 157
[10] Johnson P A V, Wright A C and Sinclair R N 1983 *J. Non-Cryst. Solids* **58** 109
[11] Susman S *et al* 1991 *Phys. Rev.* B **43** 11076
[12] Wang Q *et al* 1992 *J. Non-Cryst. Solids* **143** 65
[13] Van Brutzel L *et al* 2001 *MRS Proc. (Boston, MA)* V3.9.1
[14] Kalia R K *et al* 2003 *Int. J. Fract.* **121** 71

[15] Lucas J P *et al* 1995 *Scr. Metall. Mater.* **32** 743
[16] Kohn W and Sham L J 1965 *Phys. Rev.* **140** 1133
[17] Hohenberg P and Kohn W 1964 *Phys. Rev.* B **136** B864
[18] Yang L H 2000 Advanced atomic-level materials design *Industrial Strength Parallel Computing* ed A E Koniges (San Francisco, CA: Morgan Kaufmann) p 297
[19] Perdew J P, Burke K and Ernzerhof M 1996 *Phys. Rev. Lett.* **77** 3865
[20] Tuckerman M E, Martyna G J and Berne B J 1990 *J. Chem. Phys.* **93** 1287
[21] Nakano A *et al* 2008 *Int. J. High Perform. Comput. Appl.* **22** 113
[22] Gropp W, Lusk E and Skjellum A 1999 *Using MPI, 2nd Edition: Portable Parallel Programming with the Message Passing Interface* (Cambridge, MA: MIT Press)
[23] Lee S and Ravichandran G 2003 *Opt. Lasers Eng.* **40** 341
[24] Zhu T *et al* 2003 *Mol. Simul.* **29** 671
[25] Feuston B P and Garofalini S H 1990 *J. Appl. Phys.* **68** 4830
[26] van Duin A C T *et al* 2001 *J. Phys. Chem.* A **105** 9396
[27] Ogata S *et al* 2004 *J. Appl. Phys.* **95** 5316
[28] Lidorikis E *et al* 2001 *Phys. Rev. Lett.* **87** 086104
[29] Takemiya H *et al* 2006 *Proc. of Supercomputing (Tampa, FL)* (Los Alamitos, CA: IEEE Computer Society)
[30] Nomura K *et al* 2008 *Int. J. Comput. Sci.* **2** 437
[31] Peng L *et al* 2008 *Euro-Par 2008—Parallel Processing* (Berlin: Springer) pp 763